ResearchGate

See discussions, stats, and author profiles for this publication at: https://www.researchgate.net/publication/353089355

Digital volume correlation for meso/micro in-situ damage analysis in carbon fiber reinforced composites

Article *in* Composites Science and Technology · July 2021

DOI: 10.1016/j.compscitech.2021.108944

CITATIONS
3

READS
126

7 authors, including:



Mahoor Mehdikhani
KU Leuven
32 PUBLICATIONS **500** CITATIONS
SEE PROFILE



Christian Breite
KU Leuven
23 PUBLICATIONS **56** CITATIONS
SEE PROFILE



Yentl Swolfs
KU Leuven
120 PUBLICATIONS **2,076** CITATIONS
SEE PROFILE



Jeroen Soete
KU Leuven
43 PUBLICATIONS **628** CITATIONS
SEE PROFILE

Some of the authors of this publication are also working on these related projects:

Fatigue crack initiation and short crack growth in Ti-6Al-4V View project

FiBreMoD View project

All content following this page was uploaded by Mahoor Mehdikhani on 20 July 2021.

The user has requested enhancement of the downloaded file.

Digital volume correlation for meso/micro *in-situ* damage analysis in carbon fiber reinforced composites

Mahoor Mehdikhani*, Christian Breite, Yentl Swolfs, Jeroen Soete, Martine Wevers, Stepan V. Lomov, and Larissa Gorbatikh

KU Leuven, Department of Materials Engineering, Kasteelpark Arenberg 44, 3001, Leuven, Belgium

Abstract

Recently, *in-situ* X-ray Computed Tomography (CT) has shown its potential for 3D damage analysis in composite materials. However, the characterization of damage in X-ray tomograms is not always straightforward, and it requires post-processing of the 3D images. In this study, we explore the potential of Digital Volume Correlation (DVC) for the detection and characterization of damage in fiber-reinforced composites, where fibers provide the required 3D speckle pattern. Preliminary analysis via "digital deformation" of 3D images is performed to verify the applicability of DVC for quantification of deformation and damage in a carbon/epoxy laminate and to estimate the measurement errors. Then, real-deformation images, acquired with synchrotron CT during *in-situ* tensile loading of the laminate, are analyzed with DVC to detect different damage mechanisms. A rough analysis is performed at the mesoscale using subset-based DVC, followed by a more detailed investigation at the microscale via finite-element-based DVC. Damage appears in the DVC strain fields as local strain magnification. Crack opening displacement can be estimated reliably via the jumps in displacement fields. DVC proves to be a promising tool for damage characterization in X-ray tomograms of fiber-reinforced composites, especially when simple methods such as grayscale thresholding are not adequate.

Keywords: A. Polymer-matrix composites (PMCs); C. Damage mechanics; D. X-ray computed tomography; Digital Volume Correlation

* Corresponding author (tel: +32 16 37 69 25 – email: mahoor.mehdikhani@kuleuven.be)

1. Introduction

1.1. *In-situ* damage analysis in composites

Different techniques for investigation of damage in Fiber-Reinforced Composites (FRCs) have been developed over the past decades [1]. Some of the damage investigation techniques can be applied *in-situ*, allowing for real-time damage analysis. For instance, optical imaging or electron microscopy can be applied during mechanical tests for live 2D monitoring of the specimen surface. The deformation and the small-scale damage mechanisms, such as fiber/matrix debonding, matrix cracking, and fiber breakage, in the consecutive images can be too small to be noted with the naked eye. Therefore, image processing techniques, such as Digital Image Correlation (DIC), are required to quantify the deformation in the images. DIC tracks the grayscale pattern, which is provided by a natural or artificial random speckle pattern on the surface. This technique is used for deformation analysis of FRCs, widely at the macro- and mesoscale (e.g. in [2, 3]) and more recently also at the microscale (e.g. in [4-6]). DIC can be utilized for characterization of any type of damage, when the damage causes a (fictitious) strain localization on the surface, which certainly occurs when the damage leads to material decohesion (e.g. in [7]). The strain localization is fictitious since it does not correspond to a real material deformation, but to the opening of damage, which causes a displacement jump. Thus, it is referred to as "strain magnification" in the current study.

In-situ microscopy coupled with DIC remains, however, a 2D surface-measurement technique. Thus, it does not allow the analysis of the deformation inside the material and different damage mechanisms happening in a multidirectional laminate. To overcome this limitation, X-ray Computed Tomography (CT) can be employed for image acquisition. Although *ex-situ* 3D investigation of damage in polymer-matrix composites has started more than two decades ago, e.g. in [8], and has been widely used, e.g. in [9, 10], *in-situ* high-resolution analysis has received increasing attention only during the past decade, thanks to improvements in Synchrotron Radiation

Computed Tomography (SRCT). SRCT allows continuous acquisition of high-resolution volumes with a very short scan time.

Characterizing damage at the micro-scale is crucial for understanding, predicting, and improving the material behavior. Grayscale thresholding has been the most common way to detect and segment cracks in (*in-situ*) X-ray tomograms of FRCs, e.g. in [11]. Although techniques to enhance thresholding segmentation and detectability of cracks have been proposed, e.g. in [12-17], they still suffer from limitations such as not revealing any information about the directionality of damage. Another issue is detecting damage when the gray-value contrast between the crack and the material is low and/or the scan resolution is insufficient to resolve the crack, which is problematic in particular when the crack opening is rather small. In fact, thresholding cannot reliably detect cracks with openings smaller than a voxel. Besides, if the damage does not cause decohesion of the material, it is not feasible to detect it via the thresholding method.

Similarly to the 2D case, a solution is to use image-processing techniques to quantify the deformation in 3D images, and thus to detect damage in X-ray tomograms. Digital Volume Correlation (DVC), a 3D extension of DIC, is a robust technique to characterize the deformation in 3D. It can be used for damage identification in the X-ray CT images, with several advantages over the thresholding method. Firstly, the abovementioned issues (i.e., low contrast between crack and material, cracks much smaller than a voxel, and damage that does not cause decohesion) are less significant for DVC. Secondly, DVC allows a more objective detection of damage, based on identifying local strain magnifications, and does not require human involvement, which is often not the case in thresholding. Thus, DVC can be used for automated damage detection. Still, the results need interpretation. Finally and very importantly, DVC can also identify the damage directionality by determining the magnified strain component, which allows categorization of the detected damage into specific damage mechanisms.

1.2. Digital volume correlation and its application to FRCs

DVC was developed in 1999 for applications in biomechanics [18]. It is a pattern recognition method, which quantifies the deformation in consecutive 3D images of a deforming object. Similarly to DIC, the deformation is quantified by tracking the grayscale pattern, but inside the material, which asks for a volumetric distinctive speckle pattern of sufficient contrast (instead of a surface pattern in the case of DIC). The images can be acquired *in-situ* or *ex-situ*, typically with (synchrotron) X-ray CT. DVC algorithms are either subset based (local) or Finite-Element (FE) based (global). Subset-based approaches divide the Volume Of Interest (VOI) into smaller volumes, called "subsets", and perform correlation independently (locally) on each subset. In contrast, FE-based approaches perform correlation (globally) over the whole VOI, thus, ensuring continuity of the displacement field, which leads to more robust and accurate results than subset-based approaches. However, FE-based DVC is computationally more expensive [19-21].

Due to the loss of displacement continuity at the boundaries of subsets, subset-based approaches usually yield poor accuracy. However, their precision is acceptable, and they are cost-effective in capturing large displacements (typically >10 voxels). Moreover, subset-based DVC can be used as an initial displacement guess for a high-accuracy FE-based DVC (explained in Section 2) [20, 21].

FE-based approaches were developed to obtain a fine and continuous displacement field. The displacement is acquired at once over the entire VOI, using parallel algorithms based on domain decomposition methods. The solution is determined by solving a set of systems of equations. For interpolation of the solution, typically, finite element discretization is used. The elements can be 8-node cubes or 4-node tetrahedrons, with first-order shape functions. The DVC output is calculated with sub-voxel accuracy at the Gauss points and then linearly interpolated at the FE nodes. FE-based approaches are computationally expensive due to the high number of degrees of freedom associated with solving a large set of systems of equations at each iteration in a

refined FE mesh. Nonetheless, the resulting field is continuous at any location and has a value at every voxel [19-21].

DVC has been used for the investigation of the deformation in FRCs in a few studies. Brault et al. [22] performed DVC on images of a unidirectional (UD) carbon/epoxy specimen under 3-point bending, acquired via conventional X-ray CT with a voxel size of 52 μm. Metallic particles were introduced in the material as speckles. Due to the large voxel size, only mesoscale displacement and strain maps could be computed. With a much smaller voxel size of 4.18 μm, Safriet et al. [23] applied DVC to a deformed image of a cylindrical UD carbon/epoxy specimen, acquired via conventional X-ray CT after longitudinal compression. At the acquired voxel size, the natural gray-scale attenuation pattern of the material was deemed to be sufficient as a speckle pattern for DVC to detect the crack. Although the authors showed some results of the crack analysis, no explanation of the crack characterization was provided.

The most extensive application of DVC to FRCs has been reported by Borstnar et al. [24], where a Mode I interlaminar crack was investigated in a UD carbon/epoxy laminate. SRCT scans were made with a voxel size of 0.32 μm, and DVC with 150-voxel (48.8-μm) subsets was performed. The discrete DVC fields did not allow accurate analysis of the crack since the correlation was poor in subsets containing a crack. Only the volume ahead of the crack could be analyzed. However, the crack tip was estimated to be the location where the correlation was lost. They found that the crack opening causes an increase in the strain component normal to the crack plane ahead of the crack tip, which decreases along the crack length.

Yet, the ability of DVC to characterize different damage mechanisms in FRCs is not explored. More specifically, a methodology for detecting cracks in X-ray tomograms using DVC, determining their directionality, and quantifying them is not established. However, there is a need for such a methodology, especially for cases where the grayscale thresholding approaches are inadequate (see Section 1.1). In the current study, the potential of DVC for the characterization of different damage mechanisms in FRCs

is explored. High-resolution 3D images are acquired via *in-situ* SRCT during loading of a carbon/epoxy cross-ply specimen. DVC fidelity in the measurement of deformation and damage of transverse and longitudinal plies is evaluated by performing a preliminary analysis. In turn, subset-based and FE-based DVC are applied to the real-deformation tomograms, which allows the characterization of the formation and propagation of different damage mechanisms at the meso- and microscale.

2. Specimen, loading, image acquisition, and DVC

The studied material is a carbon/epoxy composite laminate with a stacking sequence of $[90_4/0_5]_s$ made from 50-μm thick prepregs of *Mitsubishi 34-700WD* carbon fibers and *736LT* epoxy, supplied by *North Thin Ply Technology*. After holding the temperature for 60 min at 70 °C, the laminate was cured for 45 minutes at 120 °C temperature inside an autoclave with 0.5 MPa pressure. A double-edge notched specimen with a notch section area of ~ 1 × 1 mm^2, shown in Fig. 1a, was cut from the cured laminate using waterjet machining, similar to [25]. The specimen was loaded in 0° tension (*z* direction), using a displacement-controlled tensile rig provided by *INSA Lyon*, with a deformation rate of ~ 1.4 μm/s. The specimen was scanned *in-situ* via synchrotron X-ray during loading. The test was performed at the *TOMCAT* beamline of the *Swiss Light Source (SLS)* in *Villigen, Switzerland*. The scans were made continuously with a beam energy of 20 kV, a propagation distance of 60 mm, and 1000 projections with an exposure time of 9 ms. The magnification was 10 times, and the voxel size was 1.1 μm. The size of a full volume was 2016 × 2016 × 1716 voxels in *x*, *y*, and *z* directions, respectively, which includes also some of the empty space around the specimen.

The scans were reconstructed into 3D volumes using an absorption-based algorithm provided by *SLS*. This algorithm can account for the deformation occurred during the scan although this deformation is very small for a scan time of 9 s. The images contain a large level of noise, especially in the transverse plies (since the fibers are almost parallel to the synchrotron beam). Therefore, a 3D “non-local means” filter with a search

window of 10 px and local neighborhood of 3 px was applied to the reconstructed images to reduce the noise. The natural texture of the material, more specifically the individual fibers, in the scans served as an adequate random speckle pattern for the analysis at the scale of interest. Hence, no particles were added to the material for speckling.

Eight volumes corresponding to the loading steps with almost the same force intervals are selected. The steps are identified as Steps 0-7 on the force-displacement curve in Fig. 1b. The volumes are registered (overlaid on top of each other), with 3D rigid transform by "Normalized Mutual Information", and resampled with "Standard" (linear) interpolation, in the commercial software *Avizo 2019.1*. The eight volumes are uploaded to *Mendeley Data* [26] for public access so that other researchers can use them for different microstructure and damage characterization techniques, and compare their results with those presented in Section 4.

Subset-based DVC is applied to the volumes, which detects local strain magnifications in the whole specimen, allowing a rough analysis of damage and suggesting the location of smaller VOIs for FE-based DVC. FE-based DVC is applied to multiple smaller VOIs that include damage, for more precise, microscale analysis. The DVC analysis is performed using module *XDigitalVolumeCorrelation* in *Avizo 2019.1*. Subset-based DVC is applied with cubic subsets of 48 px (≈ 53 μm) per side, while FE-based DVC is performed using tetrahedral elements of 16 px (≈ 18 μm) per side. The sizes are chosen based on the analysis of the radial autocorrelation of the microstructure, as explained in the software guideline [21]. The subset-based DVC is applied using a "correlation" metric with a "threshold" of 0.7, while only "translation" transformation is allowed. The FE-based DVC runs with a displacement "Convergence Criterion" of 0.001 px, which determines the required displacement evolution during one iteration for fulfilling the convergence.

For the mesoscale subset-based DVC (Section 4.1) and the microscale damage interaction FE-based DVC (Section 4.2.1), an image at each step is correlated with the

(first) reference image. For the microscale crack analysis FE-based DVC (Section 4.2.2), however, the correlation is done incrementally with the preceding step. This is to allow capturing the large crack opening between two consecutive steps.

DVC works better if an initial displacement field from a preceding step or from a rougher DVC analysis is fed into the new analysis, as an initial guess for the algorithm. Thus, for the mesoscale subset-based DVC with 48-px subsets, the resulting displacement field of each step (correlated with Step 0) is used for the following step (Fig. 2a). For the microscale damage interaction analysis (Section 4.2.1) and the preliminary analysis (Section 3), the resulting displacement field of the subset-based DVC on Step n and Step 0 is fed into a subset-based DVC on Step n+1 and Step 0. Then, the resulting displacement field of the latter is used in an FE-based DVC on Step n+1 and Step 0 (Fig. 2b). For the microscale crack analysis FE-based DVC (Section 4.2.2), which is incremental, three consecutive DVC initializations are made, each providing the displacement initialization for the next one. For any Step n+1, firstly, a 48-px subset-based DVC is performed on Step n-1 and Step n, followed successively by a 48-px subset-based DVC and a 48-px FE-based DVC on Step n and Step n+1. The resulting displacement of the latter serves as initialization for the final 16-px FE-based DVC (Fig. 2c).

3. Preliminary DVC analysis

Prior to correlation of the acquired volumes, a preliminary analysis is performed to 1) check whether the chosen DVC parameters are suitable, 2) estimate the accuracy and precision of DVC (by analyzing the measurement error), and 3) examine whether DVC can detect a damage-like feature in an image. This preliminary analysis includes “digital deformation”, “rigid body”, and “digital crack formation”. The analysis is conducted on microscale cubic VOIs of 200 × 200 × 200 px^3 (≈ 220 × 220 × 220 μm^3) size from the longitudinal plies, called “longitudinal VOI”, and from the transverse plies, called “transverse VOI” (Fig. 3a and b). Both VOIs are analyzed in the following sections, but

detailed analyses are explained only for the transverse deformation of the transverse VOI as this type of deformation is of greater importance in the current study. The scheme for the digital deformation and digital crack formation is presented in Fig. 3. For each deformation and damage case, either the displacement or the strain field is shown for the sake of space, but the selection is made such that the entire figure is qualitatively representative of different features in the DVC fields.

3.1. Digital deformation

To assess the accuracy of DVC for deformation quantification, the applied deformation should be known. This known deformation is provided, here, via digital resizing of the 3D image. To this end, cubic VOIs of the Step 0 volume are digitally deformed (resized) in the *ImageJ* software, using the bicubic resampling method. Both VOIs are enlarged for 4 px (= 2% strain) in two directions: the longitudinal and transverse directions, creating in total four digital deformation cases. DVC is applied to each deformed VOI and its corresponding reference VOI. Since the applied deformation in this analysis is supposedly uniform, the resulting strain is ideally expected to be uniform throughout the entire VOI.

The corresponding strain fields shown in Fig. 3e and f exhibit some irregular non-uniformity on the surfaces of the volume, which are deemed to be measurement artifacts due to poor image correlation at the VOI boundaries. To prove this, the calculated ε_{zz} of each element is plotted versus its x-coordinate in Fig. 4a and b for the case of transverse deformation of the transverse VOI, as a representative example. This is performed for the 1) entire VOI (Fig. 4a), 2) entire VOI excluding the first surface elements (Fig. 4b), and 3) entire VOI excluding the first and second surface elements (not shown due to similarity to Fig. 4b). The outliers noted in Fig. 4a do not exist in Fig. 4b. The data becomes more uniform by removing the “false” surface values, which is evident by calculating the strain Standard Deviation (SD) in the three cases, i.e. 0.21%, 0.15%, and 0.16%, respectively. The last two values do not show a significant difference. Thus, to

remove the “surface error” from the FE-based results, the first surface elements are excluded hereafter.

After filtering out the surface values, the average and SD of the resulting strains, respectively providing an estimation of the accuracy and precision of the analysis, are calculated and presented in Table 1 for the four deformation cases. The average values are within 2.01 – 2.03%, which is very close to the applied digital strain of 2%, and the SDs are within 0.04 – 0.18% of strain, which is quite low.

The strain fields of all four cases (two of them presented in Fig. 3g and j) reveal that the measured strain is not uniform along the deformation direction. More specifically, periodic high- and low-strain strips are observed. They are attributed to the resampling during digital resizing, where the gray values of the pixels in the resized image are obtained via bicubic interpolation. Their correlation with the pixels of the reference image results in the periodic strips in the strain field, which are deemed to be image-processing artifacts. The number of periods, i.e., four, correlates with the number of pixels added to the reference image. To visualize this more clearly, ε_{zz} profiles along the deformation direction (normal to the periodic strips) are plotted in Fig. 4c for the case of transverse deformation of the transverse VOI. The values can be approximated by a sine function centered around the applied strain, i.e. 2%. Although the strain average is close to the applied strain, the SD is still affected by the interpolation artifact. Since the resulting SDs contain (small) interpolation errors, they can be considered as overestimates of DVC measurement errors. It should be noted that these overestimates do not account for the physical errors in real-deformation images.

To check whether the selected FE mesh size is suitable, a mesh sensitivity analysis is performed using the digitally deformed transverse VOI. Four element sizes are chosen: 10, 16, 26, and 36 px. The resulting strain averages, presented in Fig. 4d, do not significantly differ for different element sizes. Since the digital deformation is not applied perfectly uniformly throughout the VOI, the resulting SD is expected to be non-zero, but its true value is not known. Higher SD for the 10-px analysis, in Fig. 4d, can

be interpreted as a higher measurement resolution, but its small difference with that of the 16-px analysis can be neglected, especially if the 100-time larger calculation time for the 10-px analysis is considered. Therefore, the 16-px (≈ 18 μm) element size that was identified based on the material microstructure will be used hereafter unless otherwise stated.

Although digital deformation analysis excludes some physical errors (e.g. imaging noise) and involves some artifacts (e.g. resampling interpolation error and noise acting as speckle pattern), it is one of the only feasible ways to apply a known deformation to a microscale VOI for investigation of the deformation measurement accuracy. This analysis also shows the importance of disregarding the surface elements.

3.2. Rigid body

As mentioned earlier, the digital deformation analysis excludes some physical errors present in real SRCT imaging. To check how DVC copes with errors in real images, a rigid body analysis is performed. For this, longitudinal and transverse VOIs are selected in two successive volumes that were captured with only 9 s difference (Step 7 and Step 7-ε in Fig. 1). The increase in applied strain in this 9 s is expected to be less than 0.05%. Each VOI is translated 10 px in longitudinal and transverse directions, making four rigid body motion cases, plus two still rigid body cases (no translation). DVC is applied to each still/translated VOI, from the Step 7, and its corresponding reference VOI, in the Step 7-ε. The resulting averages and SDs over the entire VOIs are reported in Table 1.

Table 1 shows that for still rigid body analysis of both VOIs, the resulting displacement averages and SDs are rather low, implying a small noise and good correlation. Only the longitudinal translation of the transverse VOI has SDs just above 1 px. The longitudinal VOI consistently yields negative average displacements. For rigid body motion analysis, the translation of 10 px is detected via DVC with a small deviation (≈ the corresponding average displacement in the still case). Most of the resulting strain averages, for both still and rigid body analyses, are close to zero. Again, the longitudinal translation of the transverse VOI has a bit higher resulting strains

(Table 1), showing lower accuracy and precision in this case. Moreover, for each VOI, DVC calculates more scatter for the strain component that is in the direction of translation. In summary, this rigid body analysis implies that DVC yields an acceptable level of error between two different scans, which include physical imaging noise, and that DVC can quantify the rigid body translation. Still, this is doubtful for longitudinal translations, which will be detailed in the following section.

3.3. Digital crack formation

After investigating the accuracy of DVC in quantifying deformation and rigid body in the SRCT volumes, its capability to detect damage is explored. For this, three analyses are performed: 1) digital mode I crack correlated with the same image, 2) digital mode I crack correlated with the preceding image, and 3) digital mode II crack correlated with both the same and the preceding image.

3.3.1. Digital mode I crack correlated with the same image

To check whether DVC can identify a mode I planar decohesion, caused by damage in the material, features representing cracks are digitally created in the cubic VOIs. The digital cracks are introduced by adding one or more black, orthogonal slice(s) (depending on the digital crack thickness) in the middle of the image stack using *ImageJ*. As shown in Fig. 3k, the digital cracks are totally planar and span through the whole volume, while a real crack has an irregular morphology and can have a variable opening over its plane. Yet, this method of introducing the digital features allows a simple evaluation of crack characterization. For both longitudinal and transverse VOIs, taken from Step 0, the additional slices are introduced in the fiber and cross-fiber directions, which mimics, respectively, intra- and translaminar cracks. DVC is applied to each (digitally) cracked VOI and its corresponding non-cracked VOI. As noted in Fig. 3g-j, the digital crack is identified with a jump in the displacement field (U) or, consequently, with a localized magnification in the strain field (ε). The strain magnifications as detected by DVC are caused by the crack openings. They are not material deformation strains, but useful for detection and characterization of damage.

Fig. 3g-j reveals that the introduced intralaminar slices are well detected, while the detection of translaminar slices is less accurate. This is most likely because DVC faces difficulties to measure, at this scale, the translation or deformation of FRCs along the fiber direction in a non-speckled FRC (due to the lack of a suitable speckle pattern along the fibers), as recognized also in [24]. This is explored by calculating the grayscale SD in windows of 9×9 px^2 in the transverse and longitudinal slices of each VOI. The sum of the SDs of all windows for the longitudinal VOI has is 1.6×10^8 and 2.0×10^8 when sliced longitudinally and transversely, respectively. For the transverse VOI, the total SD is 0.9×10^8 and 1.4×10^8, respectively. These numbers reveal more texture in the transverse slices. The difference is more significant for the transverse VOI.

A crack size analysis, i.e. measuring the Crack Opening Displacement (COD), is performed for the digital intralaminar cracks in the transverse VOI. To this end, cracks with six different CODs are mimicked by inserting black planar features in the middle of the image stack with six different thicknesses: 1, 4, 8, 16, 32, and 48 px. Correlating each case with the reference VOI using a 16-px-element FE-based DVC, it is noted that the strain magnifications corresponding to the crack openings exaggerate the COD (Fig. 3). To investigate this, the ε_{zz} profile along a line passing through the center of the VOI and normal to the crack plane is plotted in Fig. 5a for different CODs. The COD results for the 48-px crack are not included, as it had extraordinary high values that would disturb visualization of other strain profiles. The surface-element values are not excluded in this figure.

Cracks appear as peaks in the ε_{zz} strain profile. As noted in Fig. 5a, for the three smallest CODs, the strain peak value correlates linearly with the COD. Fig. 5c indicates this linear correlation for small CODs more clearly. For the 16- and 32-px cracks, the relationship deviates from linearity. For the 48-px crack, two strain peaks are observed.These peaks are four orders of magnitude larger than those of the smaller cracks, implying a large analysis error for the largest COD. It can be concluded that the

strain peak values correlated to the COD only for cracks with a COD smaller than the FE-based-DVC element size.

For none of the cracks, the width of the peaks correlates with the COD (Fig. 5a). The peak width is more or less constant for the first three CODs, suggesting that it only depends on the DVC element size. This is investigated by performing a mesh sensitivity analysis for the case of 1-px COD, with element sizes of 10, 16, 26, and 36 px. The ε_{zz} strain profiles presented in Fig. 5b confirm that the width of the strain peak is a function of the element size. This figure also shows that for a given COD, the smaller the DVC element, the larger the peak value will be. In other words, the slope of the linear relationship in Fig. 5c depends on the element size.

Measuring COD via strain is not a direct measurement and needs interpretation. DVC resulting displacement is used to quantify the COD of the digital cracks. For each case, the COD is determined with the difference in the normal-to-crack-plane displacement of the two sides of the crack, referred to as the displacement jump height. Fig. 5d shows that for the four smallest cracks, the displacement jump nearly equals the thickness of the digitally introduced features. For the two largest cracks, which are larger than the element size, the measured CODs are not accurate anymore. The mesh sensitivity results, presented in Fig. 5e, imply that the COD measured by the displacement jump is insensitive to the element size.

Another way that can be potentially used for detection of cracks in FE-based DVC is via the “correlation residual”, i.e. an image that is the difference between the reference image and the deformed image corrected by the DVC calculated displacement field. A crack is identified as a dark strip in a residual slice normal to the crack plane (Fig. 5f and g), due to the difference that the crack makes in the deformed image. The residual analysis reveals that although the width of the residual strip looks less exaggerated than the width of the high-strain strips, the residual profile analysis along a line normal to the crack plane could not provide quantitative data on COD, especially for the larger cracks. Therefore, the results are not shown here. It should be noted that the presence of cracks

in the deformed image hinders the FE-based DVC to converge completely. However, the lack of convergence occurs only for the crack region (when the crack is not very large), and for the rest of the volume, the correlation is performed correctly.

It can be concluded that DVC can detect cracks with openings not larger than the element size. If the COD is very large, DVC cannot track the deformation at the crack region anymore. Since the cracked and the reference image are nearly the same, this analysis leaves out the potential physical errors between two consecutive scans. However, this allows to isolate the effect of crack size in DVC damage characterization. The next section presents a similar (but briefer) analysis including the physical error.

3.3.2. Digital mode I crack correlated with the preceding image

The same analysis as in the previous section is performed, but the cracked and non-cracked VOIs are taken from two different (but with negligible loading difference) images, to include the physical error in capturing different images. For this, the digital crack is introduced to the VOIs of Step 7, which are correlated with corresponding VOIs of Step 7-ε. Fig. 6 compares the digital crack identification in the case of correlation with the same and with the preceding image using the displacement and strain profiles along a line passing through the center of the VOI and normal to the crack plane, for the transverse VOI. The displacement jumps and strain peaks in Fig. 6a-d reveal that the digital crack can still be detected via DVC when correlating with a different image. Due to the presence of physical imaging error, the displacement jumps and strain peaks are less distinct. In particular, the profiles are less accurate for the translaminar crack (Fig. 6b and d), which is most probably due to less texture in the longitudinal slices as explained in the section before. The difference between the correlation with the same image (perfect case) and with a different image (more realistic case) is quantified with a Root Mean Square Error (RMSE) analysis. The RMSE between the displacements of the two cases is 0.40 px and 1.28 px, respectively, for the intralaminar and translaminar crack and between the strain of the two cases is 0.71% and 5.34%, respectively. The larger second number in each pair proves less accurate

DVC along the fibers. The results for the longitudinal VOI are analogous and not shown here for the sake of space.

3.3.3. Digital mode II crack

To assess the capability of DVC in dealing with shear damage, mode II cracks are digitally simulated by splitting the VOI in two and move the two parts across each other. The move can occur along the fibers (intralaminar shear crack) or across them (translaminar shear crack) in each of the longitudinal or transverse VOI. The cracked VOI in each case is correlated once with the same, non-cracked VOI (taken from Step 0) and once with the preceding VOI (Step 7 and 7-ε with negligible loading difference). The results for the transverse VOI are presented in Fig. 6e-h. For the case of correlation with the same image, the shear crack is well detected with a distinct jump in the displacement profile and a peak in the shear strain profile. However, the results for the case of correlation with the preceding image are as good as those for the mode I crack, implying that shear analysis seems to be more sensitive to real-life error and noise. The profiles of the longitudinal VOI look a bit more accurate, especially for the translaminar shear crack (due to more texture in transverse slices), but not shown here for the sake of space.

The preliminary analysis confirms that the natural fibrous microstructure of the composite can serve as the required speckle pattern for DVC, at least to quantify 2% strain and cracks between 1 px and the element size, when deformation occurs across the fibers.

4. Real-deformation DVC analysis

In this section, the real-deformation volumes acquired at different time steps during the loading of the specimen (Fig. 1b) are investigated. First, the entire specimen is analyzed via subset-based DVC for a rough mesoscale analysis to detect damage, and then smaller VOIs are chosen for detailed microscale characterization of the damage via

FE-based DVC. The full-size volumes and the small VOIs for detailed analysis of damage interaction are uploaded to *Mendeley Data* [26] for public access.

4.1. Full-size damage analysis – subset-based mesoscale DVC

The eight full-size volumes, corresponding to Steps 0 to 7 identified in Fig. 1b, with a size of $1 \times 1.4 \times 1.5$ mm^3 (x, y, z), are analyzed via subset-based DVC with 48-px (≈ 53-μm) cubic subsets. Each step is correlated with the first (reference) step. The resulting strain fields of Steps 1 to 6 are shown in Fig. 7. The fields feature some local strain magnifications that are interpreted as damage in the material (as explained in Section 3.2). Each image in Fig. 7 presents 3D fields of the three strain components (ε_{zz}, ε_{xx}, and ε_{yy}) at the same time. Each strain component can reveal damage with its opening plane orthogonal to the axis corresponding to that component. More specifically, ε_{zz} is used for detection of transverse cracks (yellow to red), ε_{xx} for delaminations (light to dark blue), and ε_{yy} for ply splits (light to dark green). To enhance the visualization of the high-strain features, strains below a certain threshold are filtered out for each component. The choice of threshold values, which determines the minimum value for the color bar, is rather subjective, but it only affects the visualization and not the analysis results. Due to the "surface error" explained in Section 3.1, the VOI boundary regions are excluded from the results.

The damage as identified in the subset-based strain fields looks quite rough, due to the rough cubic mesh of 53 μm, which is larger than the opening of the majority of the damage. Moreover, the discontinuity of the subset-based approach leads to less accurate results. Therefore, it is probable that some damage is not (accurately) detected. Nevertheless, the subset-based approach allows a (relatively) fast and rough investigation of the damage locations and magnitude in the whole specimen, which can also serve as an initialization for the following more robust and detailed FE-based DVC.

The analysis of the subset-based strain fields (Fig. 7) leads to the following observations. The first detected damage is a transverse crack in the outer 90° plies, which appears at Step 2 (see Fig. 1b). The *xz* slice shown in the zoom-in for Step 2

confirms the presence of the detected crack. At the next analysis point, i.e., Step 3, i) the first transverse crack opens more, ii) another transverse crack is detected in the other 90° plies, iii) a delamination seems to initiate from the first transverse crack, and iv) a ply split appears in the 0° plies. At Step 4, i) a delamination initiates from the second transverse crack, ii) another transverse crack shows up in the other 90° plies, iii) another ply split forms at the other side of the 0° plies, and iv) the other detected damage grows. At Step 5, no new damage is identified, but the previously detected damage develops. At Step 6, most of the detected damage vanishes. This is attributed to the weakness of DVC in dealing with cracks that have excessive openings, more specifically larger than the element size (Section 3.2). The excessive opening of the transverse cracks and delaminations can be observed in the *yz* slice of Step 6. The damage disappears even more in Step 7, which is not shown in Fig. 7 for the sake of space.

Although subset-based DVC does not reveal the exact shape of damage, the general damage configuration as well as the damage directionality and mode can be perceived from the detected strain magnifications. It should be noted that since the visualization threshold and the minimum and maximum limits of the strain fields are kept the same for all loading steps, some small damage may be absent in the images, especially for the first loading steps.

4.2. Detailed damage analysis – FE-based microscale DVC

FE-based DVC allows more accurate analysis since the mesh is finer (16-px tetrahedrons), and continuity of displacement fields is ensured (except for the crack that causes real displacement discontinuity). However, this is achieved at a higher computational cost. Therefore, smaller VOIs are chosen based on the subset-based DVC results so that they include damage. Two VOIs are chosen for detailed microscale damage analysis: one for the investigation of interaction between different damage mechanisms and one for crack analysis, which are indicated in the semi-transparent volume rendering of the specimen with the blue and red boxes in Fig. 7, respectively.

4.2.1. Interaction between different damage mechanisms

The developed DVC approach can be used to study how different types of cracks (transverse, interlaminar, splitting, etc.) interact with each other in function of the applied load. The VOI for the damage interaction analysis (the blue box in Fig. 7) consists of both transverse and longitudinal plies and is chosen such that it includes all the three types of damage. Its size is $330 \times 580 \times 630$ μm^3 (x, y, z). The VOI is truncated from all eight volumes and analyzed via FE-based DVC with a 16-px ($\approx$ 18-μm) element size. The resulting strain fields of Steps 2 to 7 are presented in Fig. 8, in the same way as for the subset-based fields, i.e. by visualizing the three strain components in one image after applying a strain threshold for each. The threshold is the minimum value for the color bar in Fig. 8. Similarly to the subset-based analysis, the first detected damage is a transverse crack appearing at Step 2, followed by a delamination and ply split at Step 4, and more damage growth at Step 5. It can be noted that the three damage mechanisms seem to be linked with each other. Again, the excessive damage at Steps 6 and 7 could not be fully detected by DVC (as explained in Section 3.2).

An advantage of FE-based DVC, apart from the detection of small-scale damage, is that it provides a more accurate representation of the crack morphology. For example, the tilt of the transverse crack is well captured by the local strain magnification. Yet, as discussed in Section 3.2, the region where the strain magnification is observed is wider than the crack opening since its width depends on the DVC element size. The crack observed at the bottom of the *xz* slice of Step 5 could not be detected via DVC. This is most likely because a part of this crack is close to the VOI boundary, where correlation cannot be performed correctly.

Moreover, the shear strain components are investigated, and it is found that the delamination and the ply split also create shear strain localization. More specifically, for all loading steps, the DVC resulting localization in ε_{xz} and ε_{yz} resembles the localization in ε_{xx} and ε_{yy}, respectively. This can be observed for Step 5, as a representative example, in Fig. 8. The shear analysis did not reveal any extra (shear) damage. Furthermore, no

shear localization could be detected for the transverse crack. An immediate conclusion can be that transverse cracks do not yield mode mixity, while delamination and ply splitting do. This requires further investigation.

4.2.2. Crack analysis

The VOI for crack analysis (the red box in Fig. 7) is chosen in the transverse plies, with a size of 230 × 770 × 385 μm^3 (x, y, z), and includes a matrix crack. It is truncated from all eight volumes and analyzed via incremental FE-based DVC. The results reported in this section correspond to the deformation occurred between two consecutive steps as the FE-based DVC is performed incrementally between two consecutive steps. Therefore, the measured CODs and strain magnifications correspond to the opening of the crack during each step and not to the total crack opening. The resulting strain fields of Steps 2 to 5 are presented in the middle column of Fig. 9 (Steps 6 and 7 are not shown due to the inaccurate detection of their excessive damage). It is observed that a transverse crack (*Crack 1*) initiates on one side of the plies, at Step 3, and propagates towards the other side, as loading increases during Steps 4. Meanwhile, another crack (*Crack 2*) starts from the other side of the plies. This can be noted in the X-ray CT and DVC resulting strain slices of Step 4 and 5, shown in the right-hand side of Fig. 9. *Crack 1* does not appear at the right-hand side of the strain field of Step 5 because incremental DVC reveals the phenomena happening only at the current step and, at Step 5, the large opening of *Crack 2* does not allow opening of *Crack 1*.

To detect the cracks via their resulting strain magnifications, the ε_{zz} of all DVC elements are plotted versus their z coordinate in the middle column graphs of Fig 8. A few small strain jumps at ~ 150 μm from the volume's top surface is noted at Step 2. The jumps become much more significant in Steps 3 to 5. These strain jumps correspond to the opening of *Crack 1*. At Steps 4 and 5, another group of strain jumps appears at ~ 230 μm from the volume's top surface, which correspond to *Crack 2*.

On the left- and right-hand sides of Fig. 9, there are graphs that represent the ε_{zz} of the DVC elements that lie, respectively, on *Slice 1* and *Slice 2*, as indicated on the strain field, versus their *x* coordinate. These slices are located at 165 μm from the left or right side of the VOI. For better visualization, strain values of the "non-crack" elements are excluded by showing only strain values above 4% (that corresponds to a 1-px crack measured by a 16-px FE-based DVC in Section 3.2, Fig. 5c). Strain values higher than 4% start to appear at Step 3, mainly for *Slice 1*, which correspond to *Crack 1*. The high-strain values are not uniform in the *x* direction, i.e. through the thickness, and increase when moving from the free surface inwards. The *Slice 2* graph at Step 3 includes only a few high-strain values since the COD of *Crack 1* is still small there. *Slice 1* graph of Steps 4 and 5 implies that the crack keeps on opening during these steps. *Slice 2* graph of these steps confirms the presence of at least one crack on the other side. For Step 4, the high-strain values correspond to the opening of both *Crack 1* and *Crack 2*, while for Step 5, they are caused mainly by *Crack 2*.

Fig. 9 also includes U_z displacement profiles along a line spanning through the mid-thickness of *Slice 1* and *2* (as indicated on the first *Slice 1*), for consecutive loading steps. As expected from the strain results, the first displacement jump occurs at Step 3, which is more pronounced on *Slice 1* than in *Slice 2*. The negative displacement values on the left side of the graph of *Slice 1* signify that the volume above *Crack 1* has moved upwards (negative *z* direction), while the volume under it, with positive U_z, has moved downwards. The displacement jump height, denoting the COD of *Crack 1* at Step 3, is ~ 5 μm. The graph of *Slice 2* shows a small COD of ~ 1 μm. The *Slice 1* U_z graphs of Steps 4 and 5 indicate that *Crack 1* opens ~ 4 μm per step. On the other side of the volume, the *Slice 2* U_z graphs show that the combined COD of *Crack 1* and *2* is ~ 8 μm per step.

To provide a validation case for the crack analysis, segmentation based on grayscale thresholding was tried. Different tools including various thresholding methods in *ImageJ* and the interactive thresholding tool in *Avizo* were tried. However, even though

the human eye sees the cracks, they cannot be detected well with thresholding. The reason is that the cracks (edges) are not very clear, and their grayscale is close to that of the matrix. This is worsened by the imaging noise in the 90° plies where fibers are parallel to the beam. To showcase this, grayscale thresholding, using Otsu's method in *ImageJ*, is applied to the crack analysis VOI of Step 5 (last DVC step). Fig. 10 shows the resulting binary image corresponding to Slice 1. Thresholding fails to provide a decent representation of the crack. A rough quantitative comparison can be made using a visual COD measurement. As can be noted in Fig. 10, a COD of 17.6 μm is measured on the U_z profile where a clear crack opening is observed. The total COD, measured by DVC as the sum of the jumps in the displacement profiles of all steps, is ~15.2 μm. For the thresholded image, it is difficult to measure the exact COD, but it seems that the crack-like feature has a COD close to the values measured visually and with DVC. This comparison shows that DVC was able to calculate an acceptable value for COD, whereas grayscale thresholding failed to do so. The fact that we cannot use thresholding to quantify the damage (at least in this case) explains and further motivates the application of DVC for damage characterization.

Different damage mechanisms could be detected in one DVC run and classified based on their magnified strain component. The detected damage mechanisms are matrix cracking, delamination, and ply splitting. DVC could detect all these mechanisms that are also visible to the naked eye in the images unless the damage is very close to the VOI boundaries. In the current study, no additional damage to what is visible to the naked eye is detected via DVC, but it is not known whether it exists either. The morphology and location of the damage can be estimated with a ± element size accuracy, and the COD can be estimated via the height of the strain jump or indirectly via the magnitude of the corresponding strain magnification.

5. Concluding remarks

DVC has been employed to characterize different damage mechanisms in tomograms of *in-situ* loaded carbon fiber-reinforced composites. The analysis of digitally deformed tomograms reveals that the natural fibrous texture of the composite can serve as the 3D speckle pattern for a DVC with 20-µm FE elements to quantify 2% of virtual strain with an accuracy of ±0.03% and a precision of ±0.18% and to detect virtual cracks between 1 px and the element size. The effect of the FE element size on DVC quantification of a uniform deformation is not significant, but it has a large impact on crack characterization. The measured strain that corresponds to the crack opening decreases with the increase in element size, and smaller elements are favorable for the analysis of the crack morphology. However, DVC with small elements is computationally more expensive and even impossible in case of a poor volumetric speckle pattern and/or a high level of noise.

Analysis of the real-deformation tomograms shows that subset-based DVC can detect different damage mechanisms, i.e., matrix cracks in transverse plies, ply delamination, and ply splits, by means of their strain magnification, and can differentiate between them by their directionality via determining the magnified strain component. Moreover, the crack mode (opening, shear, mixed mode) can be deduced from the magnified strain component. FE-based DVC enables a more accurate and detailed characterization of the damage mechanisms. In addition to their directionality and mode, FE-based DVC can provide an estimation of the location and morphology of the cracks, although it is limited by the element size. The COD can be measured via the DVC displacement jump throughout the crack plane. The micro-scale quantification of damage can address some of the present challenges in material characterization, e.g. in measuring fracture toughness.

Compared to grayscale thresholding, as a common damage detection method for 3D images, DVC has the advantage of determining the directionality and mode of the damage. Moreover, DVC can still detect a damage even if no crack opening occurs, like

in a mode II crack, while thresholding fails to do so in this case. Finally, when the crack yields insufficient grayscale contrast with the material and/or the crack opening is small compared to the scan resolution, thresholding fails to detect the crack, whereas DVC may still detect it, as the case shown in Fig. 10.

To enhance DVC damage characterization, improvements are needed in the mesh sensitivity of the damage analysis via DVC, and the less accurate measurement of translation or deformation in the fibers' longitudinal direction. A higher resolution analysis asks for the introduction of a volumetric speckle pattern to the material that can be achieved with nanoparticles. The cross-ply laminate with 90° plies on the surface are not as common as the $[0_n/90_m]_s$ configurations in real applications. However, they yield a higher level of transverse cracking and, consequently, more delamination, which made them a safe choice for this methodology development study. Other layups can be further investigated with this methodology with no extra consideration. The SRCT volumes are made available to public [26] for further analysis and comparison by other researchers.

Acknowledgments

The study is funded by the *KU Leuven Research Council*, project *C24/17/052* and *FWO Postdoc Fellowship*, project *ToughImage* (*1263421N*). It is also supported by the European Union's *Horizon 2020* research and innovation program under the *Marie Skłodowska-Curie* grant agreement *No. 722626* in the framework of the *FiBreMoD* project. We acknowledge the *Paul Scherrer Institut, Villigen, Switzerland* for provision of synchrotron radiation beamtime under proposal number *20161157* at the *TOMCAT beamline X02DA* of the *SLS* and would like to thank C. Schlepütz for assistance. Additional support to optimize the acquisition settings of the beamline was provided by I. Sinclair from *University of Southampton*. The *in-situ* testing rig was kindly provided by E. Maire from *INSA Lyon*. The software support of Dr. K. Madi from *3Dmagination Ltd* is greatly appreciated. The support of the *KU Leuven XCT Core Facility* is

acknowledged. S.V. Lomov holds *Toray Chair for Composite Materials* at *KU Leuven*, support of which is gratefully acknowledged too.

References

1. Sause, M.G., *In situ monitoring of fiber-reinforced composites: theory, basic concepts, methods, and applications*. Vol. 242. 2016: Springer.
2. Lomov, S.V., D.S. Ivanov, I. Verpoest, M. Zako, T. Kurashiki, H. Nakai, J. Molimard, and A. Vautrin, *Full-field strain measurements for validation of meso-FE analysis of textile composites.* Composites Part A: Applied Science and Manufacturing, 2008. **39**(8): p. 1218-1231.
3. Oz, F.E., N. Ersoy, M. Mehdikhani, and S.V. Lomov, *Multi-instrument in-situ damage monitoring in quasi-isotropic CFRP laminates under tension.* Composite Structures, 2018. **196**: p. 163-180.
4. Canal, L.P., C. Gonzalez, J.M. Molina-Aldareguia, J. Segurado, and J. Llorca, *Application of digital image correlation at the microscale in fiber-reinforced composites.* Composites Part a-Applied Science and Manufacturing, 2012. **43**(10): p. 1630-1638.
5. Mehdikhani, M., M. Aravand, B. Sabuncuoglu, M.G. Callens, S.V. Lomov, and L. Gorbatikh, *Full-field strain measurements at the micro-scale in fiber-reinforced composites using digital image correlation.* Composite Structures, 2016. **140**: p. 192-201.
6. Mehdikhani, M., A. Matveeva, M.A. Aravand, B.L. Wardle, S.V. Lomov, and L. Gorbatikh, *Strain mapping at the micro-scale in hierarchical polymer composites with aligned carbon nanotube grafted fibers.* Composites Science and Technology, 2016. **137**(Supplement C): p. 24-34.
7. Mehdikhani, M., E. Steensels, A. Standaert, K.A.M. Vallons, L. Gorbatikh, and S.V. Lomov, *Multi-scale digital image correlation for detection and quantification of matrix*

cracks in carbon fiber composite laminates in the absence and presence of voids controlled by the cure cycle. Composites Part B: Engineering, 2018. **154**: p. 138-147.

8. Bathias, C. and A. Cagnasso, *Application of X-ray tomography to the nondestructive testing of high-performance polymer composites*, in *Damage Detection in Composite Materials*. 1992, ASTM International.
9. Schilling, P.J., B.R. Karedla, A.K. Tatiparthi, M.A. Verges, and P.D. Herrington, *X-ray computed microtomography of internal damage in fiber reinforced polymer matrix composites.* Composites Science and Technology, 2005. **65**(14): p. 2071-2078.
10. Tan, K.T., N. Watanabe, and Y. Iwahori, *X-ray radiography and micro-computed tomography examination of damage characteristics in stitched composites subjected to impact loading.* Composites Part B: Engineering, 2011. **42**(4): p. 874-884.
11. Moffat, A.J., P. Wright, J.Y. Buffière, I. Sinclair, and S.M. Spearing, *Micromechanisms of damage in 0° splits in a [90/0]s composite material using synchrotron radiation computed tomography.* Scripta Materialia, 2008. **59**(10): p. 1043-1046.
12. Garcea, S.C., M.N. Mavrogordato, A.E. Scott, I. Sinclair, and S.M. Spearing, *Fatigue micromechanism characterisation in carbon fibre reinforced polymers using synchrotron radiation computed tomography.* Composites Science and Technology, 2014. **99**: p. 23-30.
13. Sket, F., M. Rodríguez-Hortalá, J.M. Molina-Aldareguía, J. Llorca, E. Maire, and G. Requena, *In situ tomographic investigation of damage development in ±45° carbon fibre reinforced laminates.* Materials Science and Technology, 2015. **31**(5): p. 587-593.
14. Yu, B., R. Blanc, C. Soutis, and P.J. Withers, *Evolution of damage during the fatigue of 3D woven glass-fibre reinforced composites subjected to tension–tension loading observed by time-lapse X-ray tomography.* Composites Part A: Applied Science and Manufacturing, 2016. **82**: p. 279-290.
15. Yu, B., R. Bradley, C. Soutis, and P. Withers, *A comparison of different approaches for imaging cracks in composites by X-ray microtomography.* Philosophical Transactions of

the Royal Society A: Mathematical, Physical and Engineering Sciences, 2016. **374**(2071): p. 20160037.

16. Gigliotti, M., Y. Pannier, R.A. Gonzalez, M.C. Lafarie-Frenot, and S.V. Lomov, *X-ray micro-computed-tomography characterization of cracks induced by thermal cycling in non-crimp 3D orthogonal woven composite materials with porosity.* Composites Part A: Applied Science and Manufacturing, 2018. **112**: p. 100-110.
17. Pei, S., K. Wang, Y. Li, D. Zeng, X. Su, J. Li, H. Yang, and X. Xiao, *Spatiotemporal characterization of 3D fracture behavior of carbon-fiber-reinforced polymer composites.* Composite Structures, 2018. **203**: p. 30-37.
18. Bay, B.K., T.S. Smith, D.P. Fyhrie, and M. Saad, *Digital volume correlation: three-dimensional strain mapping using X-ray tomography.* Experimental mechanics, 1999. **39**(3): p. 217-226.
19. Roux, S., F. Hild, P. Viot, and D. Bernard, *Three-dimensional image correlation from X-ray computed tomography of solid foam.* Composites Part A: Applied Science and Manufacturing, 2008. **39**(8): p. 1253-1265.
20. Buljac, A., C. Jailin, A. Mendoza, J. Neggers, T. Taillandier-Thomas, A. Bouterf, B. Smaniotto, F. Hild, and S. Roux, *Digital volume correlation: review of progress and challenges.* Experimental Mechanics, 2018. **58**(5): p. 661-708.
21. *Avizo User's Guide*. 2019, Thermo Fisher Scientific.
22. Brault, R., A. Germaneau, J.-C. Dupré, P. Doumalin, S. Mistou, and M. Fazzini, *In-situ analysis of laminated composite materials by X-ray micro-computed tomography and digital volume correlation.* Experimental Mechanics, 2013. **53**(7): p. 1143-1151.
23. SAFRIET, S., T. QUICK, D. MOLLENHAUER, and C. RYTHER. *Three-Dimensional Analysis of Damage Propagation in Unidirectional Polymer Composites Using X-ray Computed Tomography and Digital Volume Correlation*. in *American Society of Composites-30th Technical Conference*. 2015.

24. Borstnar, G., F. Gillard, M. Mavrogordato, I. Sinclair, and S. Spearing, *Three-dimensional deformation mapping of Mode I interlaminar crack extension in particle-toughened interlayers.* Acta Materialia, 2016. **103**: p. 63-70.
25. Swolfs, Y., H. Morton, A.E. Scott, L. Gorbatikh, P.A.S. Reed, I. Sinclair, S.M. Spearing, and I. Verpoest, *Synchrotron radiation computed tomography for experimental validation of a tensile strength model for unidirectional fibre-reinforced composites.* Composites Part A: Applied Science and Manufacturing, 2015. **77**: p. 106-113.
26. *In-situ synchrotron computed tomography images of a tensile test on a carbon fiber-epoxy composite for mechanical damage analysis*. 2020: Mendeley Data.

Table 1. Resulting averages and SDs over the entire VOIs for the digital deformation and rigid body analysis.

	Case	Transverse displacement average (px)	Transverse displacement SD (px)	Longitudinal displacement average (px)	Longitudinal displacement SD (px)	Transverse strain average (%)	Transverse strain SD (%)	Longitudinal strain average (%)	Longitudinal strain SD (%)
Transverse VOI	Longitudinal deformation	0	0	**2.25**	**1.01**	0	0	**2.03**	**0.11**
	Transverse deformation	**2.25**	**1.01**	0	0.07	**2.01**	**0.15**	0	0.25
Longitudinal VOI	Longitudinal deformation	0	0	**2.25**	**1.01**	0	0	**2.01**	**0.18**
	Transverse deformation	**2.25**	**1.01**	0	0.01	**2.03**	**0.04**	0	0.05
Transverse VOI	Still (no translation)	0.20	0.21	0.52	1.08	0.13	0.69	0.27	3.93
	Longitudinal translation	0.21	0.22	**10.57**	1.08	0.13	0.70	0.25	**4.42**
	Transverse translation	**10.21**	0.22	0.55	1.09	0.21	**0.84**	0.22	4.27
Longitudinal VOI	Still (no translation)	-0.55	0.27	-0.59	0.30	-0.03	1.08	-0.04	0.92
	Longitudinal translation	-0.55	0.28	**9.38**	0.36	-0.03	1.12	-0.11	**1.48**
	Transverse translation	**9.45**	0.28	-0.60	0.32	-0.04	**1.32**	-0.08	1.04

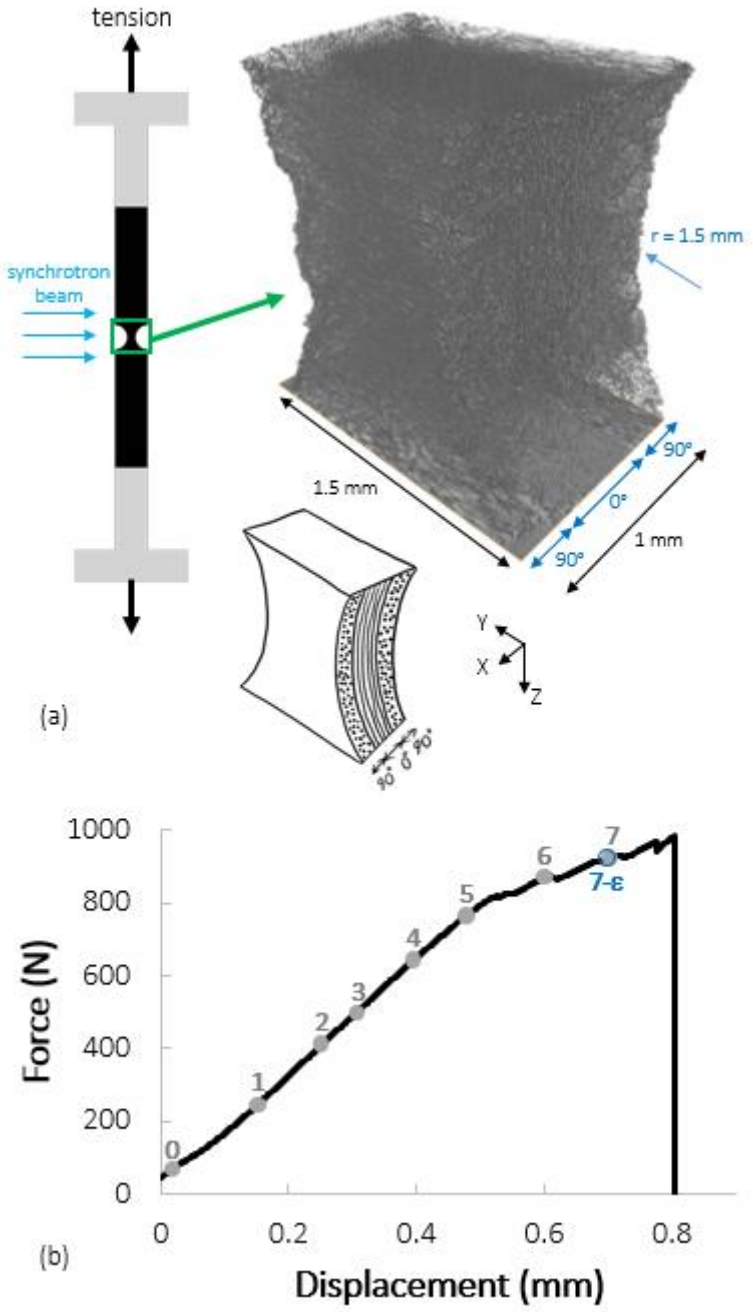


Figure 1. In-situ tensile test during synchrotron scanning: (a) the double-edge notched specimen, represented with schematics and volume rendering, (b) the force-displacement curve – the marked points (called steps) correspond to the loadings where the 3D volumes are selected for DVC, and the Step 7-ε is used for the preliminary analysis explained in Section 3.

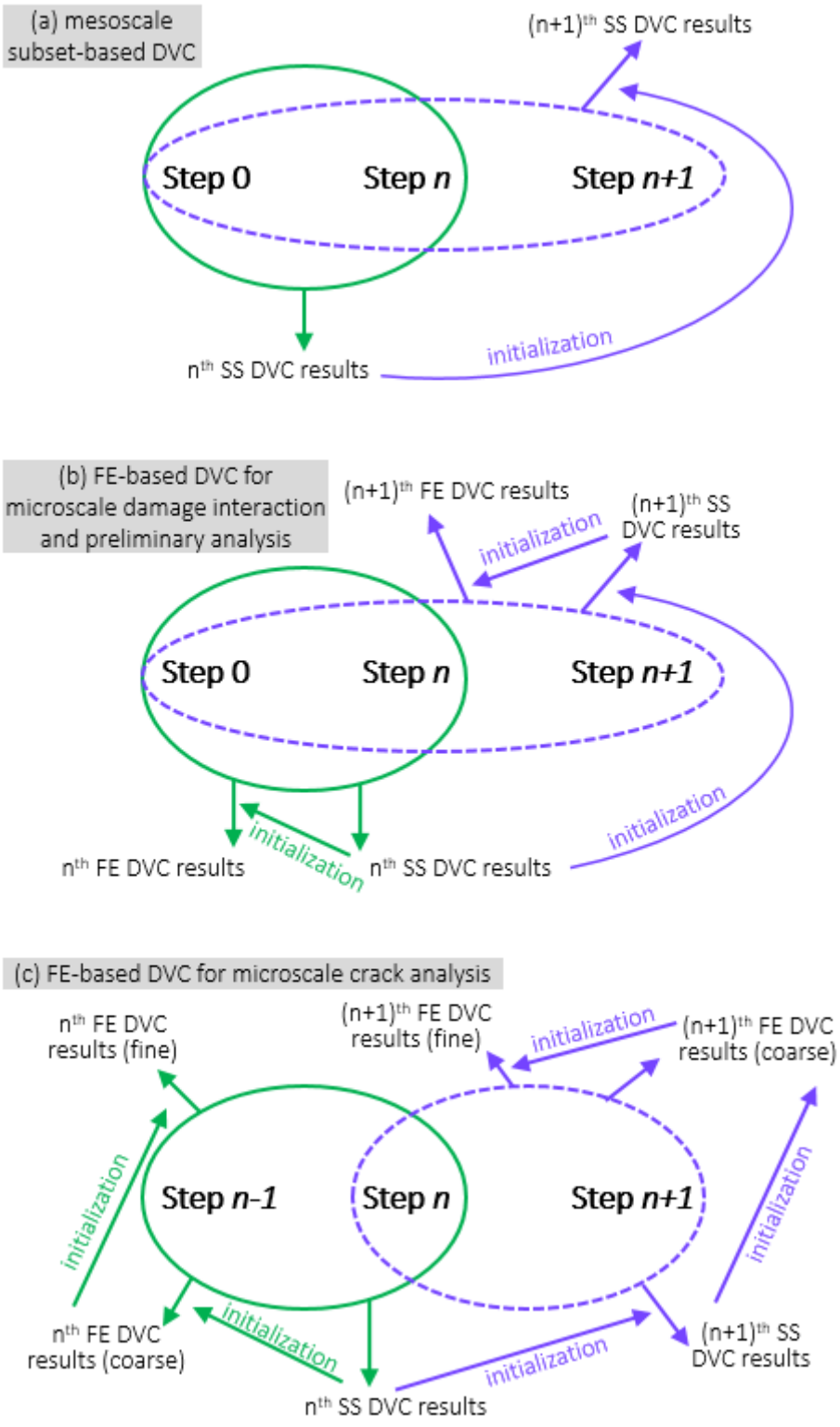


Figure 2. Displacement initialization procedures for different DVC scenarios in the current study.

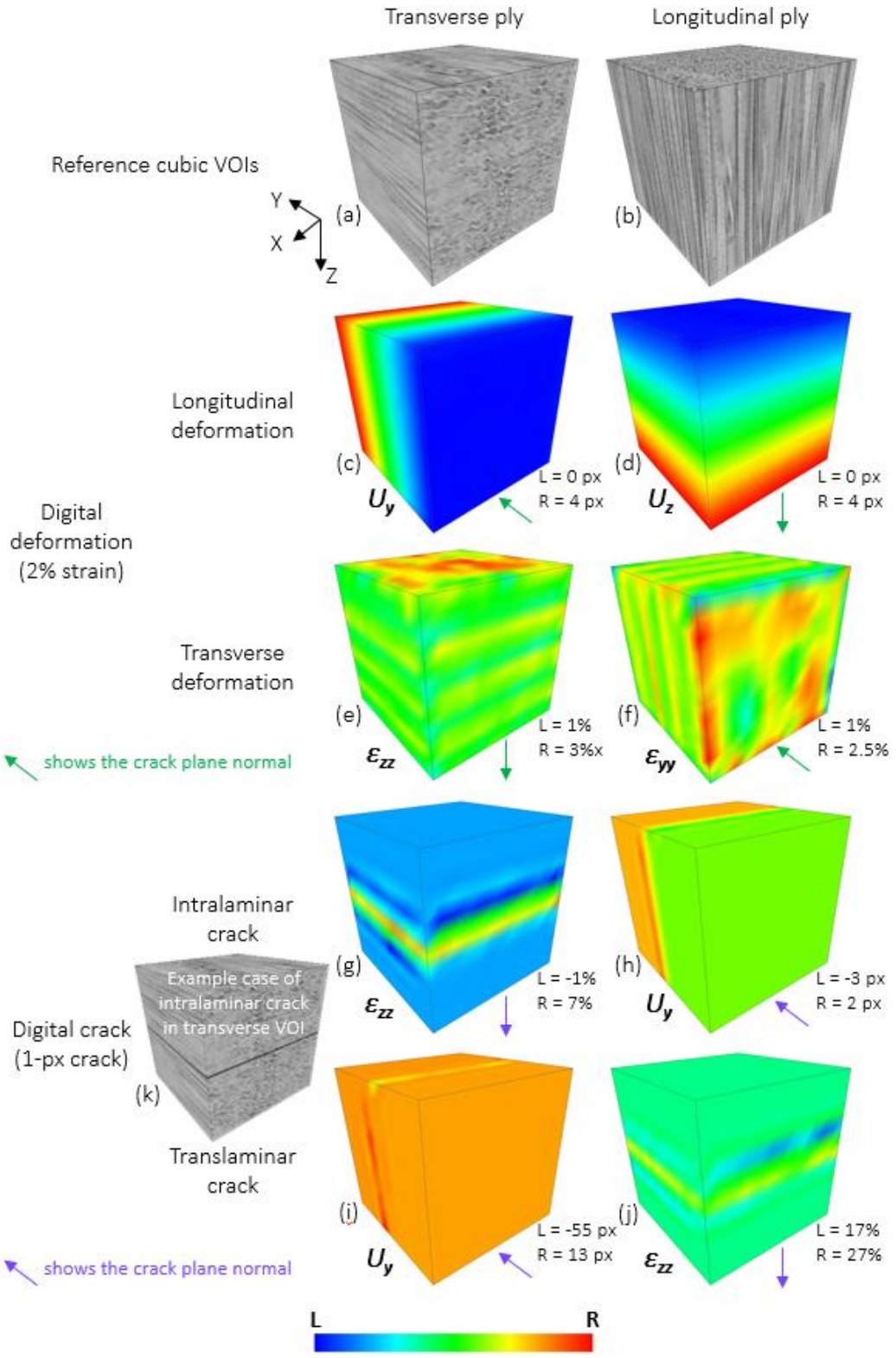


Figure 3. FE-based DVC displacement (U) and strain (ε) fields resulting from the preliminary analysis on cubic VOIs of transverse and longitudinal plies – the presented fields in c-f correspond to 2% longitudinal and transverse digital deformation and those in g-j correspond to 1-px intra- and translaminar digital cracks; L and R are the left and right limits of the color bar, respectively; the first surface elements including false values are not yet removed from the fields.

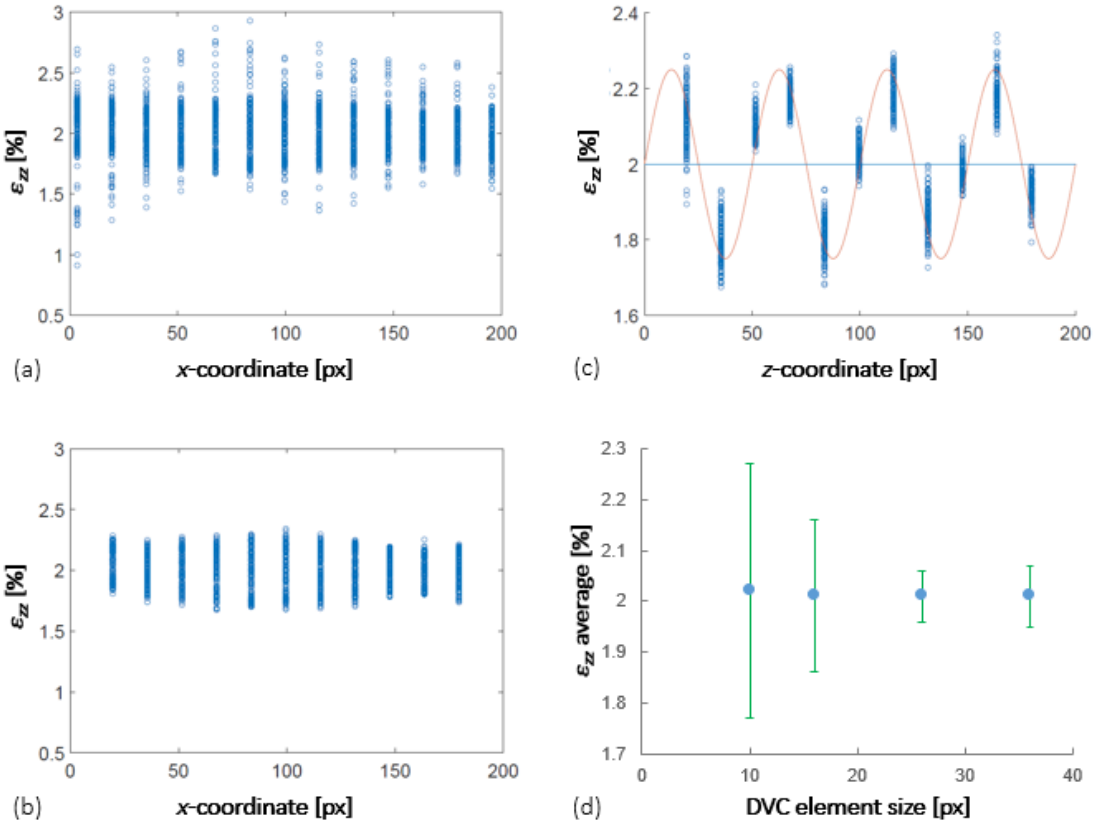


Figure 4. ε_{zz} for the case of transverse deformation of the transverse VOI (Fig. 2e) measured using FE-based DVC versus the *x*-coordinate (a) of all the elements, (b) excluding the first surface elements, and (c) versus the *z*-coordinate, i.e. the deformation direction (normal to the periodic strips in Fig. 2e) – the sine curve approximates the strain vs. *z*-coordinate data; (d) effect of DVC element size on the corresponding resulting average and standard deviation – 1 px = 1.1 µm.

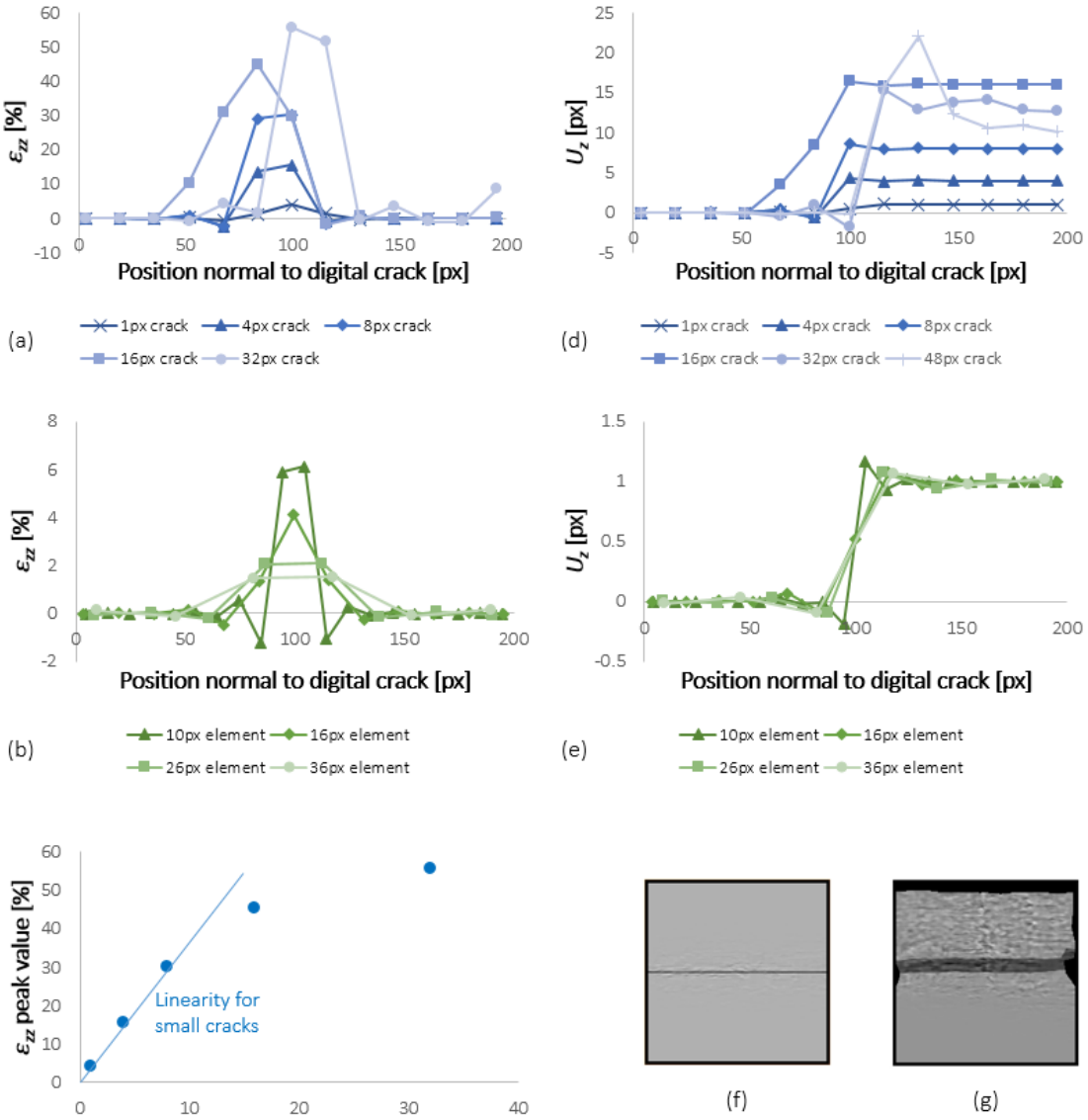


Figure 5. (a) and (d): respectively, ε_{zz} and U_z profiles along a line passing through the center of the VOI and normal to the plane of digital cracks with different CODs (constant element size = 16 px); (c) correlation between the strain peak value and the COD for an elements size of 16 px; (d) and (e): respectively, ε_{zz} and U_z profiles for the 1-px digital crack obtained with different element sizes; (f) and (g) respectively, the correlation residual slices for the 1-px and 32-px digital cracks – all data is obtained via FE-based DVC and corresponds to the case of digital intralaminar crack in the transverse VOI (like Fig. 2g) – 1 px = 1.1 µm.

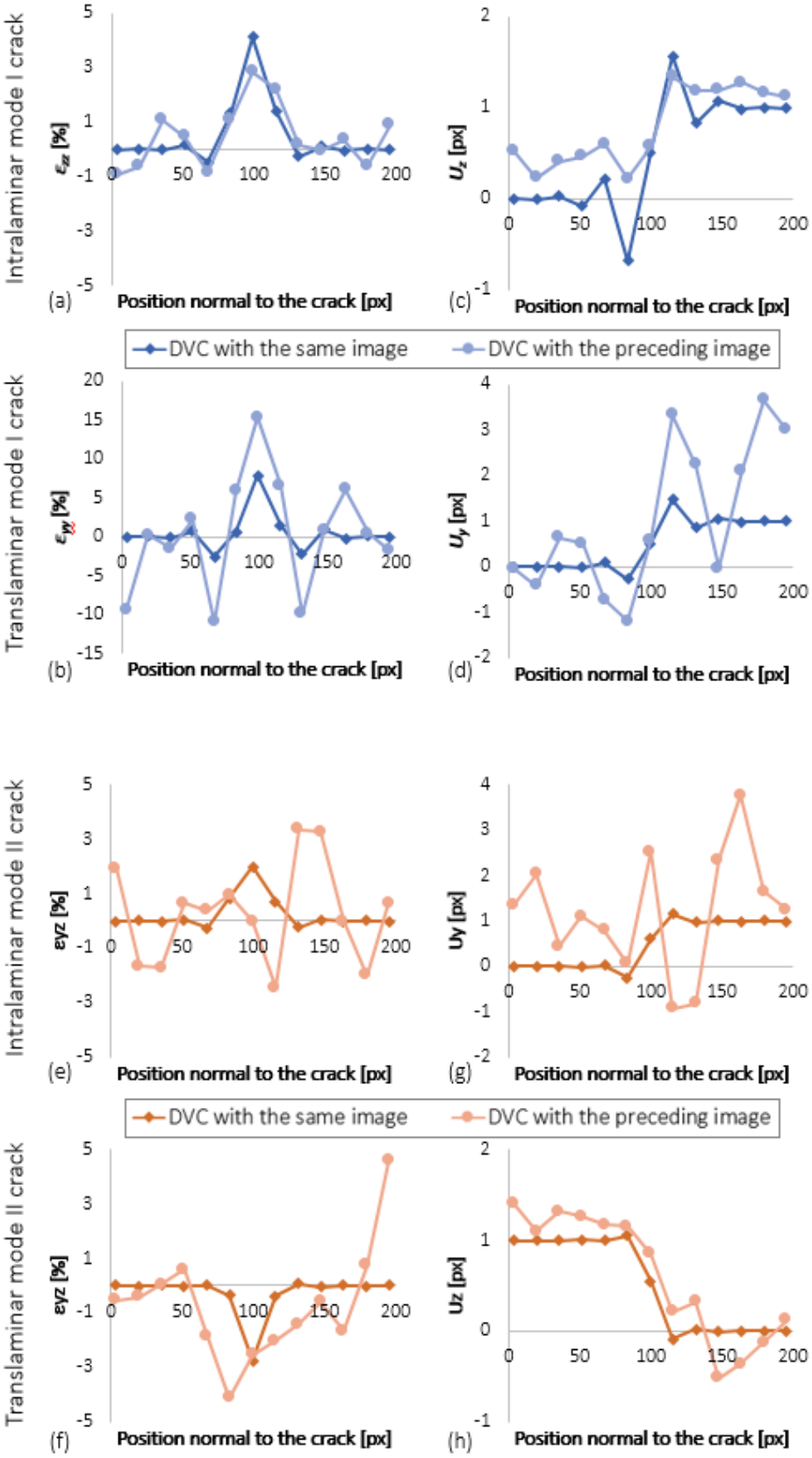


Figure 6. Strain and displacement profiles along a line passing through the center of the transverse VOI and normal to the plane of digital cracks, obtained using FE-based DVC for intra- and translaminar (a)-(d) mode I and (e)-(h) mode II cracks; each graph compares the results of the correlation with the same image (perfect case) and with a different image (more realistic case) – 1 px = 1.1 µm.

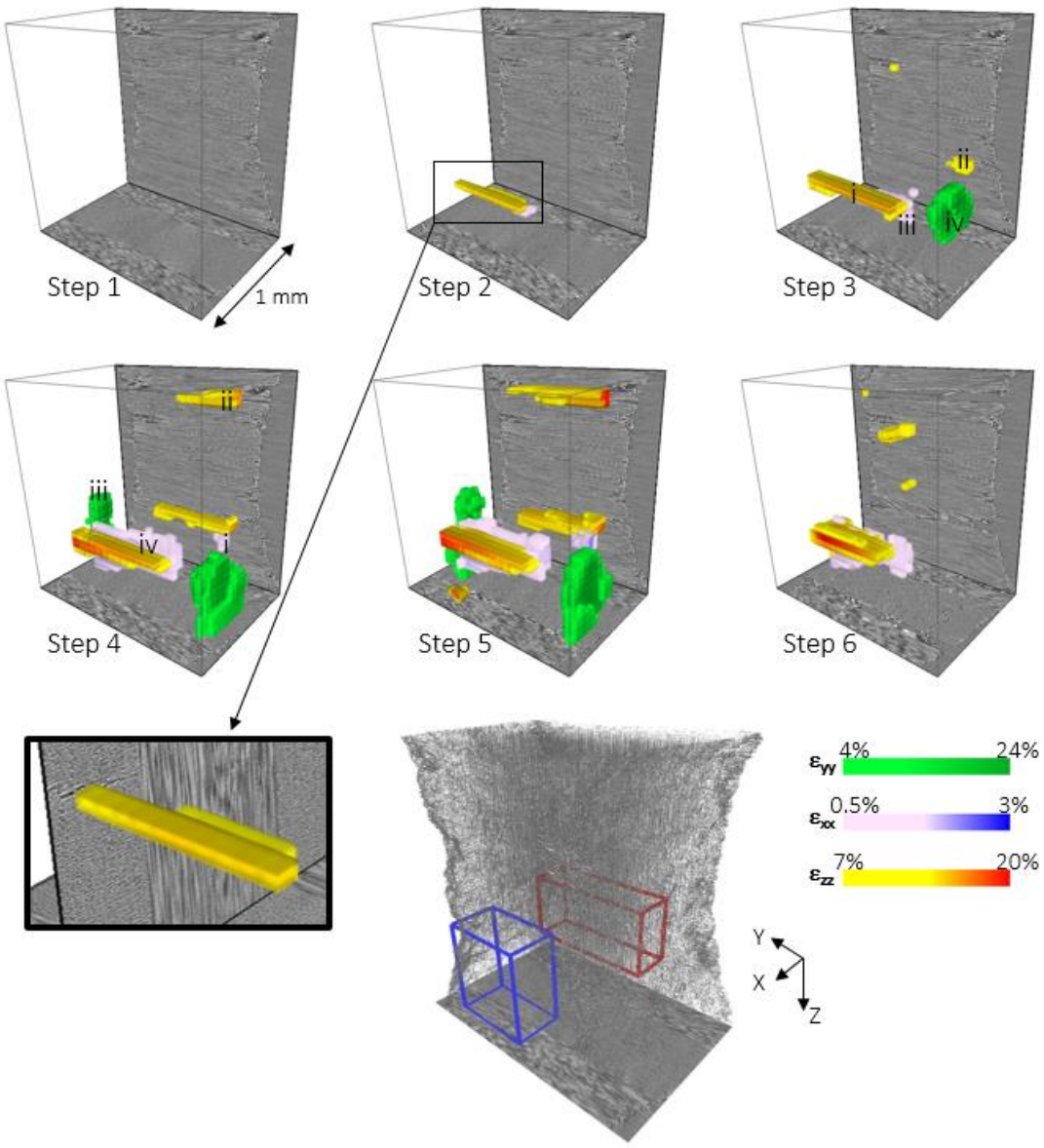


Figure 7. Strain fields of the consecutive loading steps obtained via subset-based DVC, where transverse cracks are identified with yellow-red in the ε_{xx} field, delaminations with light-dark blue in the ε_{yy} field, and ply splits with light-dark green in the ε_{yy} field – the blue and red boxes show the position of VOIs selected for detailed analysis of damage interaction and matrix crack, respectively – the tensile loading is applied in the *z* direction.

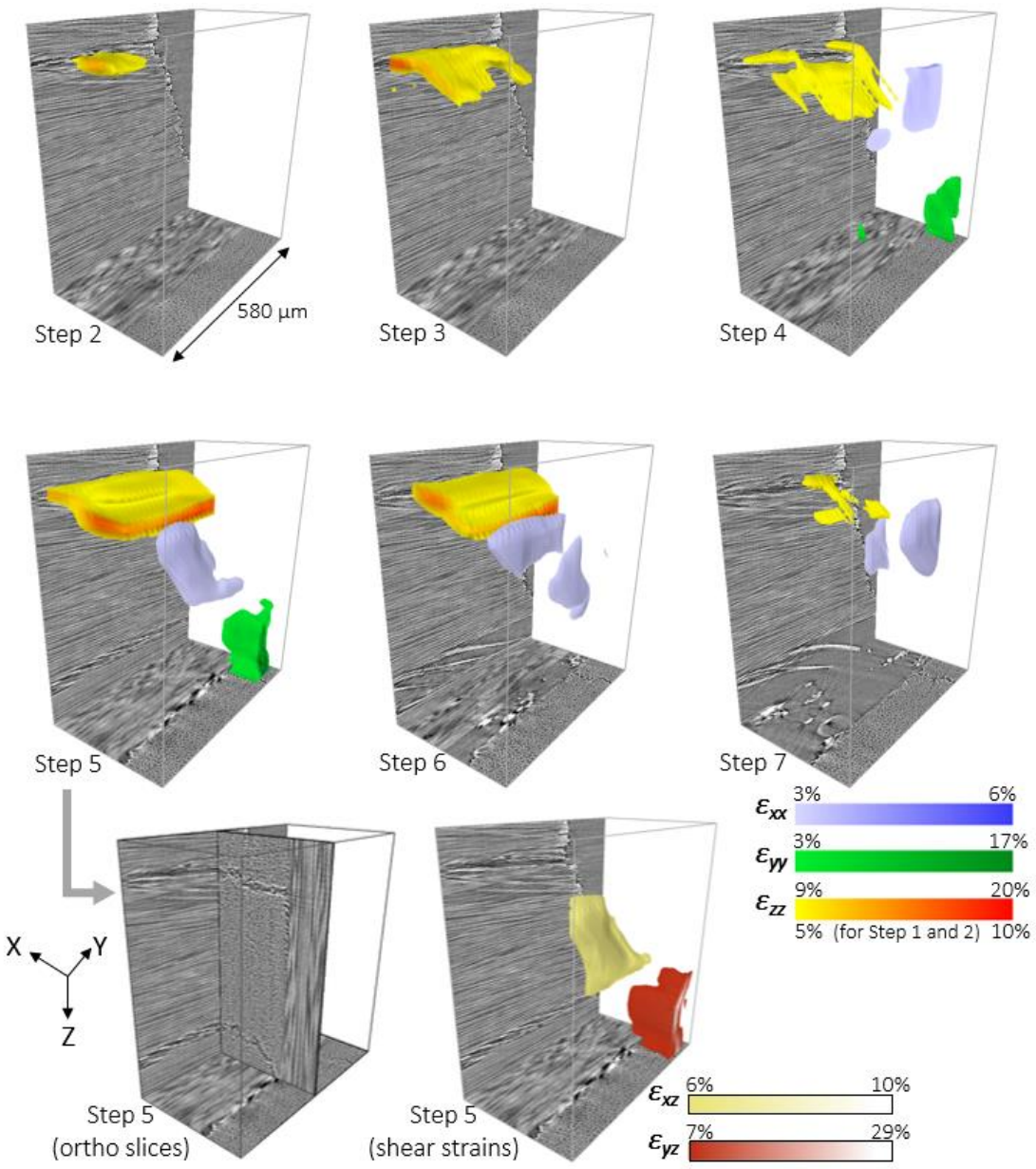


Figure 8. Strain fields of the VOI selected for detailed analysis of damage interaction (the blue box in Fig. 6) in consecutive loading steps obtained via FE-based DVC, where transverse cracks are identified with yellow-red in the ε_{xx} field, delaminations with light-dark blue in the ε_{yy} field, and ply splits with light-dark green in the ε_{yy} field; shear strain fields, ε_{xz} and ε_{yz}, are shown for Step 5 since for the other steps, as for Step 5, they resemble the fields of ε_{xx} and ε_{yy}, respectively.

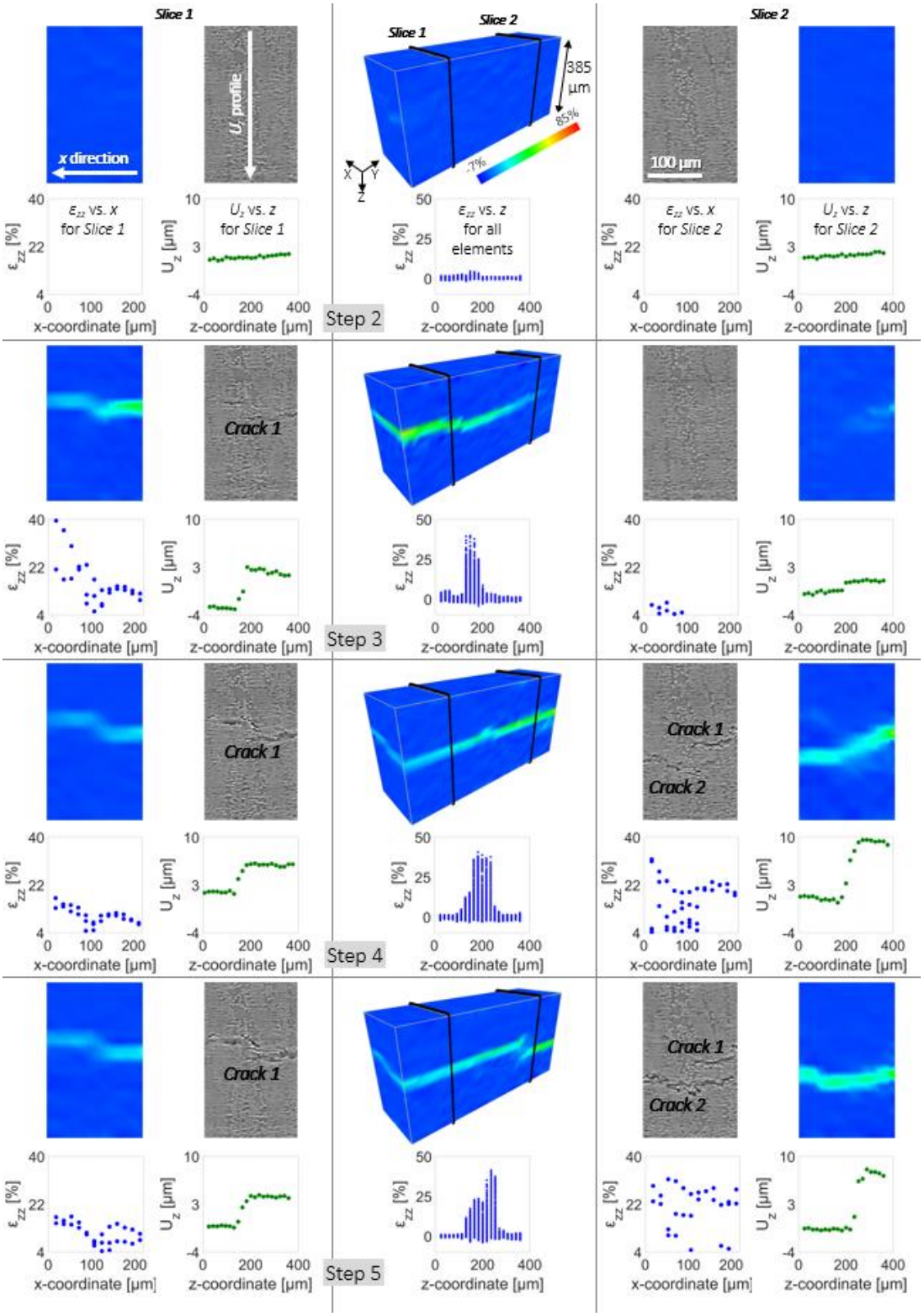


Figure 9. Middle column: strain field of the crack analysis VOI (the red box in Fig. 6) in consecutive loading steps, where the transverse crack is detected as a high strain (green-yellow) region in the strain map and a peak in the graph of ε_{zz} of all DVC elements versus their *z*-coordinate; right and left column: X-ray CT and DVC resulting strain slices on *Slice 1* and *Slice 2* (of which the position is shown on the strain field), ε_{zz} of the DVC elements on these two slices versus their *x*-coordinate, and U_z profiles along a line spanning through the mid-thickness of *Slice 1* and *2* (as shown on the first *Slice 1*), denoting the displacement jump height for COD measurement.

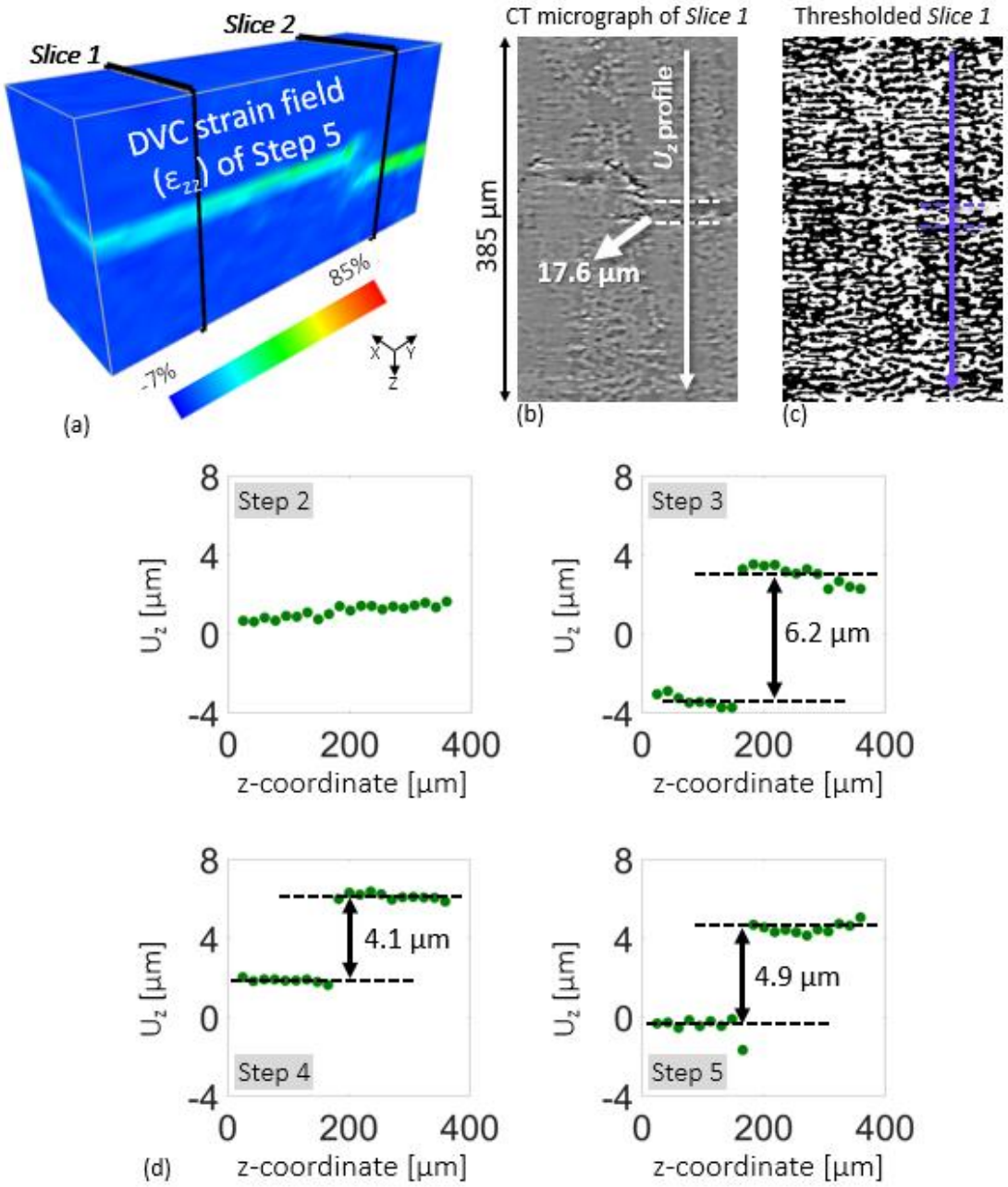


Figure 10. (a) DVC resulting strain field of Step 5, (b) visual COD measurement on the CT micrograph of *Slice 1*, (c) COD estimation on the thresholded image of *Slice 1*, and (d) DVC resulting U_z displacement profiles along the line shown on (b) for Steps 2-5. The COD measured visually on (b) is 17.6 µm and calculated by DVC as the sum of the jumps in the displacement profiles of all steps is 6.2 + 4.1 + 4.9 µm = 15.2 µm; the thresholded image does not provide a good representation of the crack.

View publication stats